**Joern-Holger Franke, Andreas Frommhold, Arnaud Dauendorffer, Kathleen Nafus, Gijsbert Rispens, Mark Maslow, "Elucidating the role of imaging metrics for variability and after etch defectivity," J. Micro/Nanopattern. Mats. Metro. 21(2) 023201 (30 May 2022) https://doi.org/10.1117/1.JMM.21.2.023201**

# Elucidating the role of imaging metrics for variability and after etch defectivity

**Joern-Holger Franke,[a,*] Andreas Frommhold,[a] Arnaud Dauendorffer,[b] Kathleen Nafus,[b] Gijsbert Rispens,[c] and Mark Maslow[c]**

[a]IMEC, Leuven, Belgium
[b]Tokyo Electron Kyushu Ltd., Kumamoto, Japan
[c]ASML Netherlands B.V., Veldhoven, The Netherlands

## Abstract

**Background:** In extreme ultraviolet lithography, maximum printable feature density is limited by stochastic defectivity. One of the methods to reduce it is the optimization of the aerial image via source mask optimization. To guide this optimization, we need to know which aerial image metric predicts defectivity. Feature variability is linked to defectivity.

**Aim:** Find which aerial image metric best predicts variability and defectivity.

**Approach:** We construct seven pupils that vary aerial image metrics [normalized image log slope (NILS), depth-of-focus (DoF), maximum intensity] in a controlled way. We measure variability and defectivity after development and after two different etch processes and correlate them to aerial image metrics.

**Results:** Stochastic critical dimension uniformity (CDU) is best predicted by NILS. Systematic CDU is determined by mask roughness through spatial frequency, with low frequencies differentiating outer and inner sigma pupils. Defectivity is best predicted by maximum intensity for missing holes and minimum intensity for merging holes. NILS and maximum intensity are strongly correlated. DoF has minimal impact.

**Conclusions:** Optimization toward maximum intensity reduces defectivity. Outer sigma pupils reduce variability. Increasing numerical aperture in next-generation EUV lithography is expected to reduce missing hole defects.



**Keywords:** EUV lithography; imaging; defectivity; plasma etch; source optimization.

Paper 21097G received Jan. 4, 2022; accepted for publication May 13, 2022; published online May 30, 2022.

## 1 Introduction

In EUV, lithography scaling is limited by defectivity. The main driver of this is stochastic variability. It can be reduced by optimizing the aerial image. Typically, this means increasing the normalized image log slope (NILS). However, it has been suggested that intensity-based metrics are a better predictor of defectivity[1,2] (Fig. 1). Also, depth-of-focus (DoF) could conceivably play a role as it leads to varying CD and NILS through the resist film. Understanding the relative importance of these parameters is of paramount importance to predict the defectivity expected for EUV imaging with a high numerical aperture (high-NA) where NILS and intensity are improved but DoF deteriorates.

To understand how defectivity depends on NILS, aerial image intensity, and DoF, three sets of illuminations were designed to vary only one of these parameters while keeping the others constant. This was possible for DoF, while intensity and NILS are generally strongly correlated. At the given pitch of 48-nm contact hole orthogonal arrays, it was possible to increase maximum

*Address all correspondence to Joern-Holger Franke, joern-holger.franke@imec.be

1932-5150/2022/$28.00 © 2022 SPIE

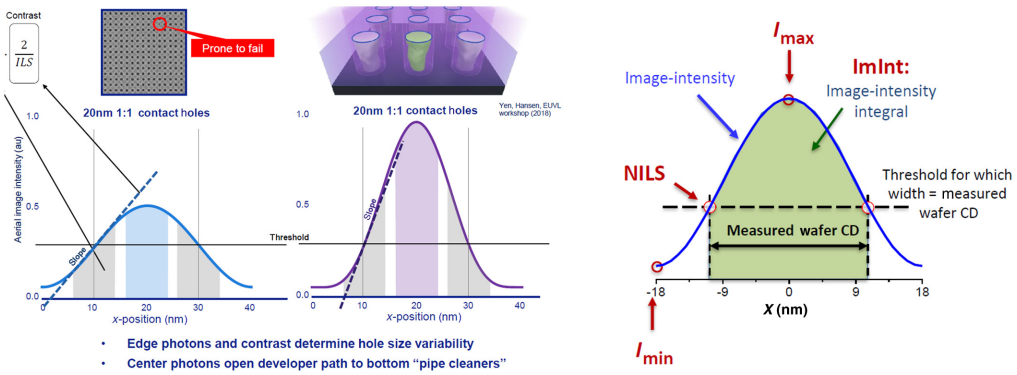


**Fig. 1** Examples from literature highlighting the role of aerial image intensity in defectivity.[1,2] $I_{max}$ denotes the highest intensity of the aerial image, while NILS is the slope of the aerial image at a certain aerial image position.

intensity at constant NILS and DoF by first increasing the number of diffraction orders captured and then increasing fading until NILS is matched.

We first correlate aerial image metrics with variability. Variability is measured as critical dimension uniformity (CDU). More specifically, we look at CDU in one part of the die (local CDU – LCDU), both ADI and after the two etch processes. To correlate to aerial image metrics, we need to decompose LCDU into stochastic and systematic components. For the systematic LCDU component, we show that pupil-specific transmission of local mask roughness needs to be considered.

Since after development inspection (ADI) metrology does not always provide the full view on defectivity and improvements to the illumination in ADI are sometimes seen to not transfer well to after etch inspection (AEI), the focus here was on the after etch defectivity. Using a contact hole defectivity vehicle and pattern transfer enabled optical defect inspection. To ensure that the pupil optimization is reliably found back in AEI, two different etch processes are studied. In this way, it is also verified whether source optimization provides additional benefits when using an advanced etch process or whether different etch processes require a different aerial image.

The outline of this paper is as follows: In Sec. 2, we demonstrate how we constructed our pupils to vary aerial image metrics in a controlled way. In Sec. 3, we summarize the experimental conditions. In Sec. 4, we bring this together by identifying correlators (or predictors) for defectivity and LCDU.

## 2 Source Optimization

The goal of the experiment was to disentangle the influence of DoF, exposure latitude (or NILS), and the maximum intensity of an aerial image on the LCDU and AEI defectivity. Therefore, the aim was to design pupils that vary only one of these parameters at a time while keeping the others constant. Overall, seven illuminations were constructed, belonging to three systematic variations [Fig. 2(a)]. The blue series (pupils 1 to 3) varied DoF at constant peak NILS and maximum intensity. The orange/red series (pupils 4/5) increased maximum intensity and peak NILS at DoF values covered by the blue series. The last variation was two pupils that differentiate peak NILS and maximum intensity (green series – pupils 6/7).

Figure 3(a) shows the number of diffraction orders that are captured through different pupil locations for regular contact holes at pitch 48 nm. To avoid complex scanner setup and asymmetric aerial images, fourfold symmetric illuminations were used throughout. Depending on where the pixels are placed, different diffraction orders are captured, leading to different aerial images. Putting a source pixel in the four-beam region gives the diffraction pattern shown in Fig. 3(b). The aerial image that results from these four diffraction orders will be dominated by spatial frequencies corresponding to the pitch itself (plus some higher frequency diagonal components). If a pixel is in the central region, the numerical aperture captures the diffraction

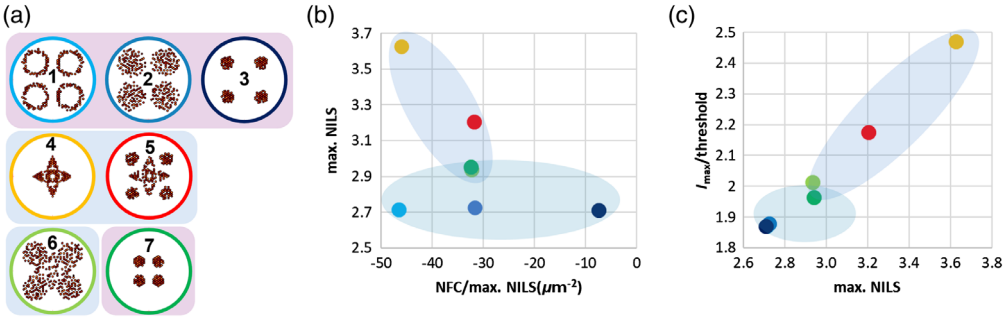


**Fig. 2** (a) Different pupils constructed. Pupils 1 to 3 vary DoF at constant peak NILS/max. intensity, pupils 4/5 maximize peak NILS and max. intensity, pupils 6/7 differentiate peak NILS and max. intensity. (b) max. NILS and NILS(focus) curvature (NFC) of all pupils. (c) max. NILS versus max. intensity (normalized to threshold-to-CD24).

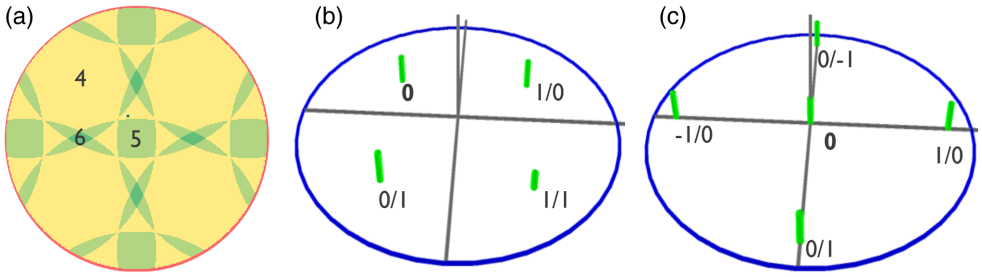


**Fig. 3** (a) Pupil map counting the number of captured diffraction orders. The specific diffraction orders captured are shown for two cases, corresponding to four-beam imaging (b) and five-beam imaging from the central region (c). 0 denotes the zeroth-diffraction order, which corresponds to the position of the source pixel in (a).

orders as shown in Fig 3(c). In this case, the presence of +/−first orders will lead to spatial frequencies in the aerial image of twice the pitch, i.e., corresponding to pitch 24 nm. This means that this aerial image will be sharper at a small CD and will have higher maximum intensity in the center of the aerial image as well as a higher image-log-slope at a small CD. These two different aerial image flavors form the building blocks of the illumination variations. Pupils 1-3 and 7 use exclusively four-beam imaging (purple ellipse in Fig. 2), while pupil 4 uses exclusively five- and six-beam imaging. Pupils 5 and 6 use a mixture of both regions (green ellipse in Fig. 2)

After selecting which diffraction orders will form the individual aerial image, the exact position of the pixel within the region for which the desired orders are captured is selected (e.g., the yellow region containing the number "4" in Fig. 3(a) which is delineated by the green regions). This position will control the through-focus behavior of the aerial image.

## 2.1 *Varying Depth-of-Focus at Constant Peak NILS and Max Intensity*

NFC or NILS (focus) curvature is the quadratic term of the NILS (focus) parabola and describes how fast NILS degrades in defocus. To construct pupils at constant peak NILS and variable NILS (focus) curvature (NFC), the position on the four-beam imaging pole is varied. An important effect is that a relative phase offset of the zeroth-order against the first-orders coming from Mask 3D (M3D) phase effects will lead to aerial image shifts of each source pixel at nominal focus.[3–7] Combining multiple pixels from the four poles of a fourfold symmetric pupil (i.e., a quasar pupil) will average out these offsets and convert them into NILS loss ("fading"). This is a two-dimensional equivalent of the effect observed for dense L/S where opposite poles show image offsets of opposite signs at nominal focus.[6,7]

Placing source pixels not at telecentric sigma (the point for which the diffraction pattern is symmetric around the optical axis), but at a distance in the pupil plane, the aerial image becomes

**Table 1** Summary of aerial image metrics for the blue or NFC series (pupils 1 to 3, target CD 24 nm).

| Pupils | peak NILS[a] | NFC/NILS[a] | NDOF (NILS>2) [a] | CD-DOF@10%EL[b] |
|---|---|---|---|---|
| 1 | 2.713 | −46.40 | 150 nm | 159 nm |
| 2 | 2.726 | −31.65 | 186 nm | 239 nm |
| 3 | 2.711 | −7.26 | >300 nm | 398 nm |

[a]from aerial image simulation.
[b]highly sensitive to chosen CD and as such susceptible to metrology offset and resist scaling effects.

nontelecentric. By displacing the source pixels along the diagonal of the pupil, the nontelecentricity can be used to compensate for the center offset at a defocus position. This would reduce NILS loss but lead to the best focus offset from nominal focus and drive down DoF as the images coming from different poles disperse more quickly through focus. Choosing pixels for which the diffraction pattern becomes symmetric (pixels at "telecentric sigma") will maximize DoF, while pixels near the edge of the yellow region of Fig. 3(a) will minimize it.

Keeping the NILS at best focus constant but decreasing DoF is achieved by symmetrizing the pupils around the telecentric sigma. The larger the distance to telecentric sigma, the higher the nontelecentricity of the aerial image coming from each pole. By pairing each nontelecentric pixel with its opposite (by constructing pupils with poles that are point symmetric around telecentric sigma) they will still lose DoF, but not gain NILS in out-of-focus conditions any longer. A pupil series starting with a dot at telecentric sigma and going stepwise towards a ring at the outer edge of the pupil will have constant NILS (and max. intensity) at decreasing DoF. This is the blue or NFC series in Fig. 2. Specific pupils are then chosen to match the NFC of the high NILS pupils (orange and red).

Table 1 summarizes the values of the NFC pupils together with the associated NDOF (DoF over which the NILS is above 2) from aerial image simulation and CD-based DoF measured on the wafers. Bear in mind that the CD-based DoF is highly dependent on the chosen CD and as such susceptible to metrology offsets as well as Bossung curvature scaling effects from the resist. As we do not have a reliable "aerial image to wafer matching" methodology the relation between NFC and CD-DoF is only tentative and solely shown for illustrative purposes.

## 2.2 *Varying Peak NILS and Imax*

The remaining pupil series vary the amount of captured diffraction orders. This will generally increase peak NILS and maximum intensity (red and orange pupils in Fig. 2). Peak NILS and maximum intensity are very closely correlating and hard to disentangle. The yellow pupil is using exclusively five- and six-beam imaging regions of the pupil to aggressively optimize for peak NILS. NILS (focus) curvature, however, increases alongside the peak NILS. This is a result of the diffraction orders effectively covering a larger portion of the NA. This pupil, therefore, generates an aerial that is closest to what we expect for high-NA imaging. It optimizes for high spatial frequency content but suffers from faster dispersion of aerial image components as well as M3D-driven fading effects.

To break the correlation of peak NILS and $I_{\max}$, we need to match the aerial image of pupils with 4-beam and 5+ beam imaging. Aerial images constructed with a different set of spatial frequencies will break the link between the slope at a certain position of the aerial image (NILS) and its maximum intensity. The challenge is however to match the NILS and NFC of this qualitatively different images. To do this we construct two pupil series (light and dark green in Fig. 4).

The first is the dark green pupil series in Fig. 4, which consists of four-fold symmetric dots that are shifted from inner sigma through the telecentric sigma to the edge of the pupil. Inner sigma hereby means sigma values smaller than the telecentric sigma. Such a pupil series will systematically trade off DoF versus peak NILS.[8,9] The underlying principle is the compensation of a pole-specific center offset by nontelecentric images in defocus. Nontelecentricity of the

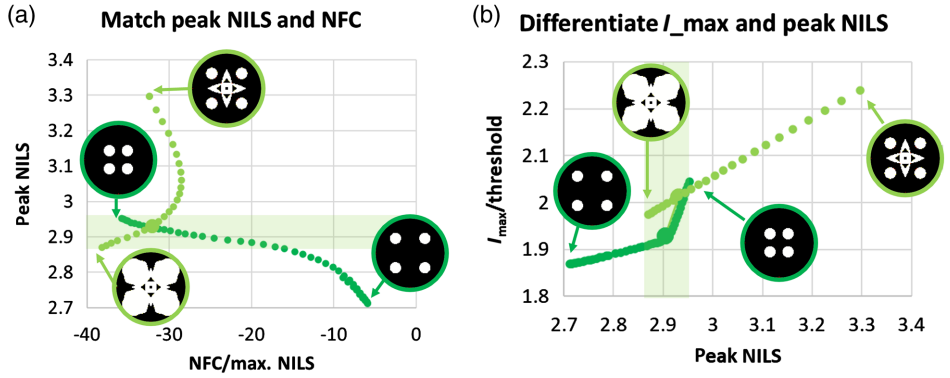


**Fig. 4** (a) and (b) Construction of green pupil series matching peak NILS and NFC while varying $I_{max}$.

aerial image from each pole increases with the distance of the dot to telecentric sigma. A high nontelecentricity will compensate for the pole-specific center offset at a small defocus value as the aerial images of opposing poles meet in defocus. The finite size of the pole will lead to dispersion of the aerial images from one pole through focus. The smaller the defocus value needed to meet the aerial image of the opposing pole, the smaller the resulting fading and NILS loss. However, larger nontelecentricities of the poles will also lead to a faster dispersion of the aerial images from opposing poles through focus. This translates into larger NFC, so pupils with high NILS will have low NFC and vice versa. The extreme case of minimal NFC and peak NILS is obtained when placing the dot at telecentric sigma (like for pupil 3 from the blue series).

The second pupil series (light green) in Fig. 4 is constructed by adding source points around telecentric sigma to the yellow pupil (pupil 4 in Fig. 2). The idea is to bring down the high NILS and NFC of the yellow pupil to intercept the dark green pupil series in Fig. 4. To this end, we want to use source points that have minimal NILS and NFC from the four-beam pole and a best focus at nominal focus. Therefore, we place these source points at telecentric sigma. The amount of source points added is then gradually increased until the four-beam poles are filled. It is evident that indeed the two pupil series intercept each other on the peak NILS/NFC plot in Fig. 4(a). In Fig. 4(b), we see that at a given NILS the pupils containing the higher spatial frequencies lead to a higher $I_{max}$. In practice, the light green pupil is very sensitive to the relative amount of four-beam to five- and six-beam imaging pixels. Multiple rounds of rendering with varying weights on the four-beam poles were required to obtain matched conditions.

Interestingly, the dark green pupil 7 has far lower minimum intensity than all other pupils (one to six). Minimum intensity is driven mostly by fading and not high spatial frequencies. This is an interesting fact to keep in mind when thinking about better image contrast afforded by high-NA to reduce defectivity: for initial, noncritical pitches using high-NA (NA 0.55), the minimum intensity will be higher than when imaging with well-optimized pupils at NA 0.33. When more diffraction orders are captured, more aerial image components from the aerial image. Due to M3D phase effects, these aerial image components are misaligned and a larger number of aerial image components makes their alignment (via source optimization) harder.

## 3 Experimental Conditions

Tools for processing and metrology are summarized in Table 2. In this study, 24 nm 1:1 dense contact hole patterns were printed with EUV lithography using a TWINSCAN NXE:3400B scanner (NA 0.33). The full layer stack is exemplified in Fig. 5. A trilayer stack consisting of a spin-on-carbon under-layer, a spin-on-glass middle layer, and a chemically amplified photoresist layer (50 nm) was coated and developed using a coater and developer tool. Patterns were transferred to a SiN layer with a plasma etch system. Two etch processes were used in this study. The first etching process used is a standard process based on lean chemistries to transfer the holes vertically into the underlying layers. A second process uses a descum step combined with

**Table 2** Tools and metrology.

| Process | Tool | Company |
|---|---|---|
| Exposure | TWINSCAN NXE: 3400 | ASML |
| Coater and developer | Coater/developer system | Tokyo Electron Ltd. |
| Etching | Plasma etch system | Tokyo Electron Ltd. |
| Defect inspection | KLA2935 | KLA |
| Defect review | EDR7380™ | KLA |
| CD measurement | CG6300 | Hitachi |

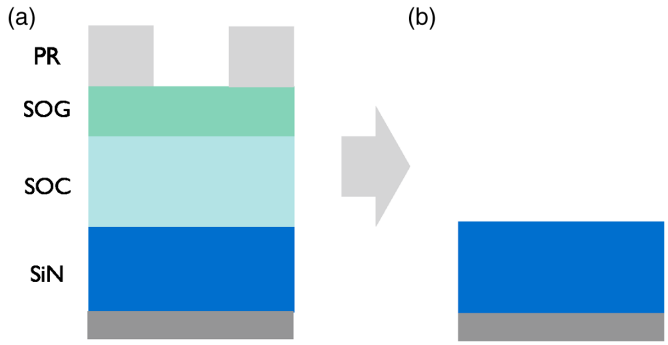


**Fig. 5** Stack at the inspection steps (a) ADI and (b) SiN open.

| Pupil | 1 | 2 | 3 | 4 | 5 | 6 | 7 |
|---|---|---|---|---|---|---|---|
| Best Energy | 94.5 | 94.6 | 94.0 | 80.8 | 87.0 | 91.9 | 91.6 |
| Max EL% | 21.6 | 22.6 | 22 | 26.9 | 24.7 | 23.4 | 23.3 |
| DOF @EL10% | 0.179 | >200nm | >200nm | 0.139 | 0.195 | 0.179 | 0.199 |

**Fig. 6** Experimental conditions and CD process window characteristics.

cycling between deposition and etching. This kind of new process helps decreasing defectivity and corrects CD variations thanks to microloading effects. CD measurements and the defect inspections were performed at ADI and AEI. Defect inspection covered the whole wafer. The field size of the exposure was adjusted so that only contact holes were printed. Different settings for sensitivity and threshold were used in the defect inspection to adjust for defectivity levels of the different etch processes. Defectivity and LCDU given in the analysis below are evaluated at individual best focus per pupil.

Figure 6 shows that the dose to print to 24-nm CD is reduced by increasing the NILS and $I_{\max}$ of the pupil. Exposure latitude increases with increasing NILS. While DoF generally follows NILS (focus) curvature. However, pupil 6 has smaller DoF then pupils 2, 5, and 7 despite the same NFC. We attribute this to the larger CD range contributing to the DoF determination, while NFC is evaluated only at target CD.

## 4 Results and Discussion

First, the LCDU for the different illuminations was examined, specifically the decomposition of LCDU into its stochastic and systematic components. The decomposition was performed as

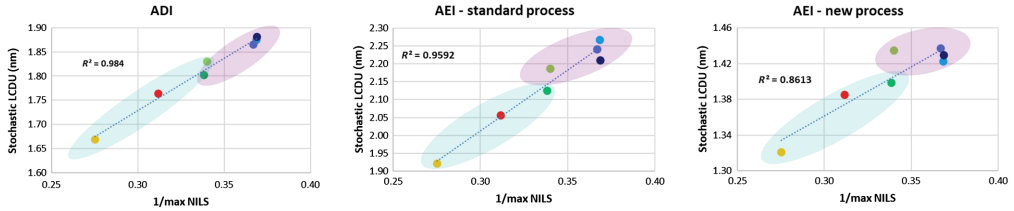


**Fig. 7** Correlation of stochastic LCDU (3 s) to maximum NILS after litho and after etch for two different processes. Ellipses color code pupils by beam count (purple: four-beam imaging only, green: containing five- and six-beam imaging source points).

described elsewhere.[10] In short, it is performed by measuring the CDs of multiple copies on wafer of the same individual contact hole from the mask. From that the systematic LCDU is calculated as 3× the standard deviation over the CD average per contact hole over all contact holes considered. By subtracting the average systematic CD per contact hole from all copies and then calculating 3× the standard variation over all contacts of all copies one arrives at the stochastic LCDU. The metrology component is determined by measuring the contacts twice and calculating 3× the standard deviation over the CD difference per contact hole between measurements 1 and 2 overall contacts divided by the square root of 2. Stochastic LCDU is then corrected for the metrology contribution by subtracting the squared values from each other. To ensure that always the same set of contact holes is measured on a wafer, the field-of-view of the CDSEM is anchored to the corners of the contact hole array. For robust results, enough contacts and copies thereof need to be included. For our analysis here 2600 individual contacts that were repeated 40 times on the wafer are measured.

LCDU provides an experimental measure of the NILS and as such is also linked to defectivity.[11] While the stochastic component characterizes the randomness in every exposure, the systematic component is part of every die and mainly attributed to the mask and reproducible effects in the scanner.

Second, we look at defectivity for the two different etch processes, as measured at appropriate sensitivity. We first look at defectivity through-hole CD for all pupils, looking at defectivity cliffs as well as the best obtainable defectivity (the "defect floor"). We compare how different aerial image metrics influence defectivity through CD as well as at target CD.

## 4.1 *Stochastic LCDU*

The stochastic part follows expectations as it correlates well with the peak NILS of the pupils (Fig. 7). While the absolute values differ for ADI and the two etch processes, the trend through the pupils is clearly visible for all three cases. For the new etch process it is slightly noisier, but the correlation is still high. Aerial image simulation was sufficient to predict the stochastic LCDU trend, no resist blur, mean-to-target for the mask making process or metrology offset had to be applied. One point of attention is the slight difference in stochastic LCDU visible for all three cases in the green series, which by design shares the same NILS and NFC. But the pupil with the higher maximum intensity has a slightly worse value. This could already indicate the relative importance of aerial image intensity.[2]

## 4.2 *Systematic LCDU*

The systematic LCDU component is impacted among others by mask roughness. This in principle means all mask features are not repeated from one unit cell to the next. The transfer of mask roughness to the wafer depends on the imaging conditions, i.e., on the pupils used. Typically, it can be approximated well by the mask error enhancement factor (MEEF), with the systematic LCDU following the simulated MEEF. This is also what we observe in Fig. 8, except for one clear outlier - the low fading inner sigma illumination (pupil 7) has a low MEEF but shows an excursion in the systematics in opposition to pupil 6. Also, the small spread in the blue series is potentially linked to the same issue as the pupils differ, but have essentially the same MEEF. We note that etch effectively reduces this spread.

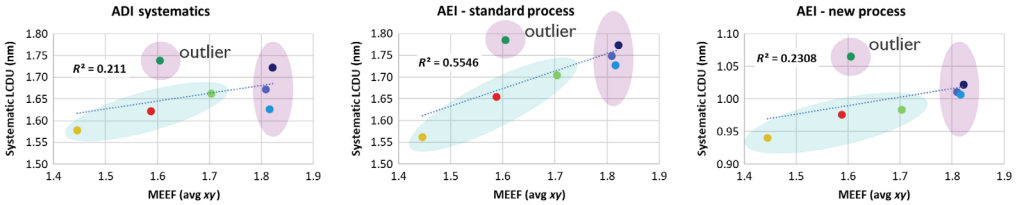


**Fig. 8** Correlation of systematic LCDU with simulated MEEF after litho and after etch for two different processes.

The larger than expected systematic roughness of pupil 7 can be explained by looking more closely at how to mask roughness transferred to the wafer. Mask roughness contains a range of spatial frequencies that can be transmitted differently through the optics.[12] In the simulation, we so far assumed a perfectly periodic mask by using only a pitch 48 nm unit cell (i.e. there is no mask roughness). The only spatial frequencies contained in this image are multiples of pitch 48 nm. The diffraction pattern, therefore, consists only of diffraction orders on a grid of $1/48$ nm$^{-1}$. Mask roughness will break this periodicity.[13,14] The diffraction spectrum of this mask would therefore contain a background of roughness-induced diffraction orders that are neglected in the periodic simulation.

How each frequency is transmitted through the optical system is then governed by the transmission cross coefficient (TCC). This function contains the information on which spatial frequencies will be transmitted by a given illumination pupil.[15] Importantly, the TCC strongly depends on the illumination pupil. It can be thought of as an illumination-dependent filter for spatial frequencies. For inner sigma pupils, all spatial frequencies can be transmitted up to a relatively large cut-off frequency. For an outer sigma pupil, certain relatively low spatial frequencies will not be transmitted. Mask roughness contains at least some components that are dominated by small spatial frequencies, e.g., multilayer roughness (correlation length ~40 nm).[16] More of this roughness will be transmitted by inner sigma pupils.

When simulating MEEF without roughness, we use a unit cell of pitch 48 nm. This leads to a diffraction spectrum only containing multiples of 1/pitch. We are therefore only sensitive to the TCC at multiples of 1/pitch. Capturing the same diffraction orders for different pupils means that we sample the (pupil-specific) TCCs only at spatial frequencies at which they are identical. Our four-beam pupils are such a case (diffraction orders captured 0, 1/0, 0/1, 1/1 for all pupils). This means that we are blind toward differences in transmission at lower spatial frequencies when we enforce periodicity at pitch 48 nm for this set of pupils.

We visualize how lower spatial frequency roughness is transmitted differently by inner/outer sigma pupils in Fig. 9. We look at roughness induced by CD-errors on the mask through the pitch to model roughness at lower spatial frequency. We increase the unit cell size in the simulation to multiples of pitch 48nm and only change the CD of only one contact hole. Using, e.g., a $2 \times 2$ array of contact holes, we perturb the mask CD and measure the aerial image CD response of only one of the four contact holes in a unit cell of pitch 96 nm, which we define as the "MEEF at supercell pitch 96." We thereby obtain an indication of how roughness of different spatial

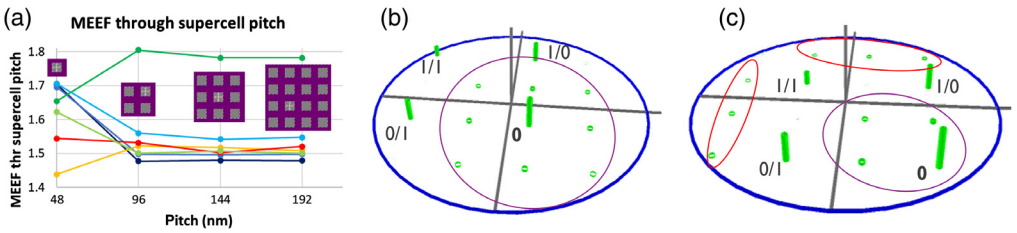


**Fig. 9** MEEF through supercell pitch. (a) shows MEEF calculated by perturbing a single contact hole in an array of increasing size (as shown in the insets). Sources are color-coded as given in Fig. 2. (b) and (c) show the diffraction spectrum at a supercell pitch of 96 nm for inner (b) and outer (c) source points. Purple circle denotes first-diffraction orders for P96 unit cell, red circle denotes third-diffraction orders.

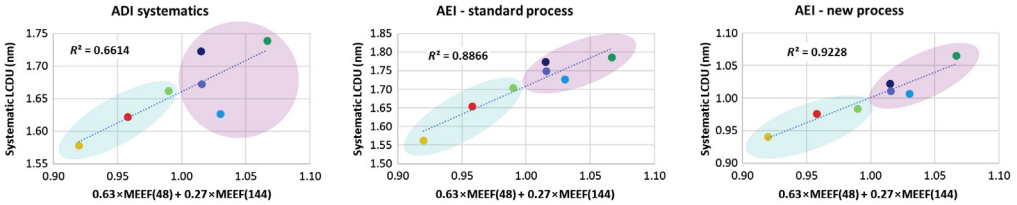


**Fig. 10** Systematic LCDU predicted by MEEF at two pitches (48 and 144 nm) after litho and after etch for two different processes.

frequencies is transmitted through the lens using an intuitive metric. Figure 9(a) shows this "MEEF" as a function of supercell pitch. A higher MEEF indicates a better transmission of roughness at the spatial frequency of 1/supercell pitch. It should be noted that due to the size of the resulting unit cells, this simulation uses a flat mask model, thereby neglecting M3D effects.

Evidently, inner sigma pupil 7 [bright green in Fig. 9(a)] shows higher MEEF at larger pitches than all other pupils. Figures 9(b) and 9(c) show the diffraction spectra of a perturbation at pitch 96 nm. Additional diffraction orders at $1/96$ nm$^{-1}$ are introduced. Importantly, the amplitudes of the first orders (inside the purple circles) are significantly larger than the amplitudes of the third orders (inside the red circles). An inner sigma source point as shown in Fig. 9(b) will capture all first orders, while an outer sigma source point will only capture 3 first orders (but more third orders). The overall amount of diffracted light in the extra diffraction orders is, therefore, higher for the inner sigma source point, which correlates to roughness in the aerial image.[13]

To improve on MEEF at pitch 48 nm as a predictor for systematic LCDU, we try to approximate the roughness into a pitch 48 nm component and a larger pitch component (we choose here supercell pitch 144 nm, i.e., a $3 \times 3$ contact hole array). The observed systematic LCDU can then be fit as a weighted sum of the two roughness components. Fitting to all three experimental data series (ADI and both AEI values) with common weights gives a relative contribution of 63% MEEF at pitch 48 nm and 27% MEEF at pitch 144 nm. Note that this fitting is distorted by the absence of M3D effects. M3D effects would, e.g., reduce the MEEF of pupil 7 relatively to the other pupils. The reason for this is that for a flat mask model there is no fading in any of these sources and the advantage of relatively lower fading of pupil 7 against the other pupils is therefore lost. An overpredicted MEEF at pitch 48 nm for pupil 7 will lead to an underprediction of the amount of lower frequency components for an optimum fit in Fig. 10. Including M3D effects would, therefore, increase the estimate of the relative amount of low spatial frequency roughness in the systematic LCDU.

## 4.3 *Defectivity*

A first assessment of the optical inspection defectivity results was done with a low sensitivity setting on focus exposure matrix (FEM) wafers. A clear ordering of the defect levels with respect to the used illumination was found at the small and large CD side where the missing and merging contacts are found (Fig. 11). This correlates well to the ranking of the pupils in terms of the maximum intensity in the center of the aerial image for the missing contacts and the minimum intensity in the dark part of the aerial image, where there is still a bit of light. It is important to assess the minimum and maximum in relation to the threshold of the print CD. The intensity plots are further normalized to the largest value to show the relative differences between the pupils. On the small CD side, the pupil with the highest maximum intensity has the lowest defect level. On the large CD side, where the minimum intensity is highest the largest defectivity is found. The ranking of the pupils with regard to defectivity is then followed well by the maximum and minimum intensity over the threshold. Note that while the yellow pupil leads the performance on missing failures, it also has the worst defectivity for merging holes due to having both the highest maximum and minimum intensity. It seems that defectivity at the defect floor around CD 26 to 27 is also smaller for the pupils with the highest maximum intensity. To confirm this, however, we optimized the experimental conditions.

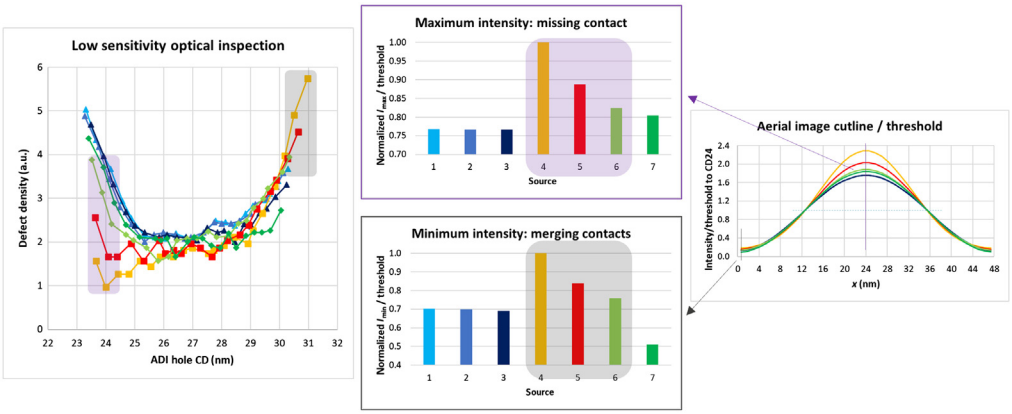


**Fig. 11** Low sensitivity optical defect inspection on FEM wafers and corresponding aerial image intensities. Defectivity (AEI) is plotted against ADI CD (left plot), indicating the different pupil ordering at small CD (missing defects) and large CD (merging defects). An aerial image intensity cutline (normalized to the threshold at CD 24) is shown on the right. The plots in the middle indicate the maximum and minimum intensity/threshold of the aerial image cutlines. Colored boxes denote the trends in Imax/threshold and Imin/threshold as well as the corresponding trends in defectivity at small and large CD in the left figure, respectively.

After optimization of the experimental conditions, it was possible to increase the sensitivity of the optical inspection to a medium setting for the standard etch process to differentiate further the defectivity performance between the pupils in Fig. 2. Different pupils show different defectivity through CD. Plotting the aerial image log slope (ILS) as a function of CD, two distinct regimes can be distinguished (Fig. 12 right). For small CDs, the pupils with the higher beam counts (green ellipse in Fig. 2 – pupils 4 to 6) have higher ILS leading to the defect cliff for the missing holes being pushed out (Fig. 12 left). The defect floor also scales with the ILS of the pupils and there is a clear ranking in terms of the defect density. But with increasing CD at a certain point the four-beam pupils (purple ellipse in Fig. 2) have a higher ILS and the ranking of the pupils for the merging failures reverses. The pupil performance is hence strongly dependent on the CD. Note that what we call "defect floor" here is just the minimum of the defectivity through CD. The fact that a higher ILS reduces defectivity at this CD [see Fig. 12(d)] could point to this not being a real defect floor, which we would expect to be illumination independent. In addition, there is some differentiation in the blue series that cannot be explained by the ILS because of the matching. Instead, the NFC appears to have a small impact on the defect floor, with the pupil with the lowest NFC (pupil 3) also having a lower defectivity.

The new etch process is very effective in reducing defectivity so that the inspection sensitivity was further increased. A similar picture of higher ILS pushing out the defect cliffs and the

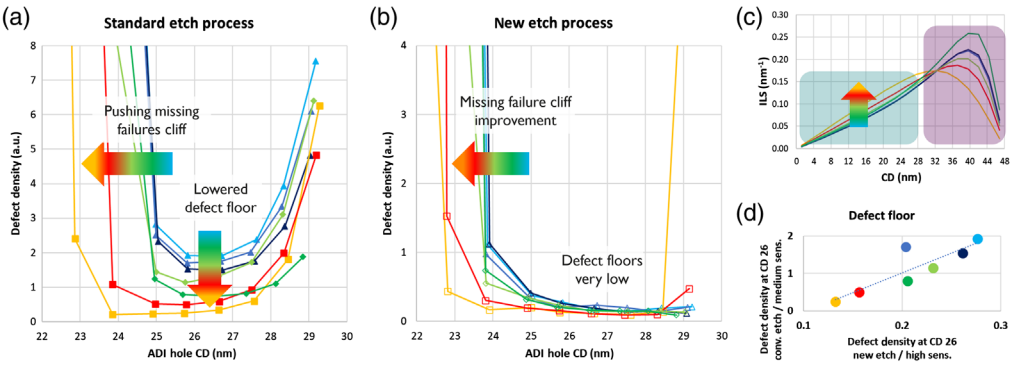


**Fig. 12** Optical defect inspection for (a) standard etch with medium sensitivity, (b) new etch process with high sensitivity setting, and (c) aerial image ILS for the illuminations versus print CD. (d) "Defect floors" at CD 26 for both etch processes [(a) and (b)].

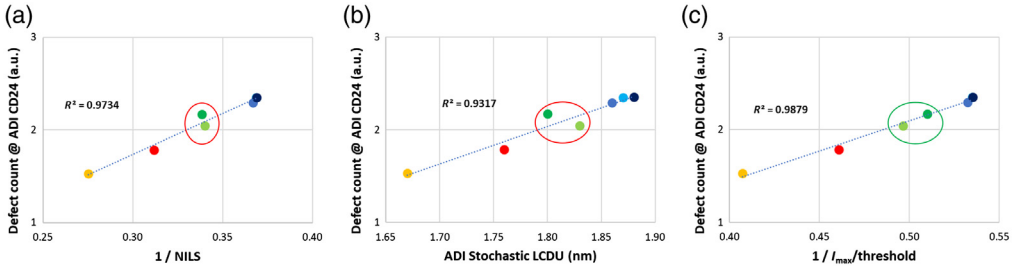


**Fig. 13** Correlation of defect rates (new etch process) to (a) NILS, (b) stochastic LCDU, and (c) maximum aerial image intensity over the threshold.

reversal in the ranking of the pupils at large CD was found (Fig. 11 middle). From this, we conclude that the benefits of the pupil optimization transferred well from ADI to AEI. In the defect floor, the new etch reduces the variability and brings down the number of defects to such an extent that it becomes difficult to distinguish the pupils. Despite this, the general trend of reduced defect count at the defect floor for the pupils with the highest maximum intensity is also visible in the new etch process [Fig. 12(d)]. A trend through NFC in the floor defectivity for the blue pupil series is not visible for the new etch, however.

In summary, defects correlate well with the maximum intensity in the aerial image in the center of the feature and the space between the features respectively. At the same time, a higher ILS effectively pushes out the defect cliffs. To answer the final question—which metrics are most predictive—the two metrics must be disentangled. Pupils 6 and 7 were designed for this purpose. Focusing on those data points in the correlation plots (Fig. 13) we see that pupil 7 (dark green) has higher defectivity. NILS does not predict this, as the two pupils were designed to have the same NILS. Hence, they fall on the same line on the horizontal axis. Also, in the defect correlation to stochastic LCDU, the higher maximum intensity pupil 6 is lower in defectivity despite having a higher stochastic LCDU value. On the other hand, correlating the defect rates to the maximum intensity, the pupils are ordered in an expected way and exhibit an almost perfectly linear trend. From this, it is concluded that the intensity over the threshold best predicts the defectivity and is deemed the most critical metric.

## 5 Conclusions

We studied a set of custom designed pupils both ADI and AEI with two different etch processes to determine which aerial image metric is the most predictive for defectivity as well as for stochastic and systematic LCDU. In summary, we find that

- Stochastic LCDU is predicted by peak NILS.
- Systematic LCDU is predicted by MEEF. When comparing systematic LCDU of inner to outer sigma pupils, the better transmission of lower spatial frequency roughness by inner sigma pupils needs to be considered.
- Defectivity is best predicted by Imax (missing holes) and Imin (merging holes).
- NILS (focus) curvature (or DoF) has a much smaller impact on defectivity than Imax. A larger DoF slightly lowers the defect floor for the standard etch, but has no such effect for the new etch.

Seven different pupils were constructed with the aim to independently vary peak NILS, NILS(focus) curvature, and maximum intensity (Imax). NILS(focus) curvature can be varied independently of peak NILS and max. intensity. However, peak NILS and Imax are strongly correlated. Breaking this correlation was possible by matching peak NILS and NILS(focus) curvature of a pupil with low spatial frequencies, but low fading and a pupil with higher spatial frequencies but higher fading.

For the systematic LCDU, there is a difference between outer and inner sigma pupils. Inner sigma pupils transmit low-frequency roughness better than outer sigma pupils. The observation

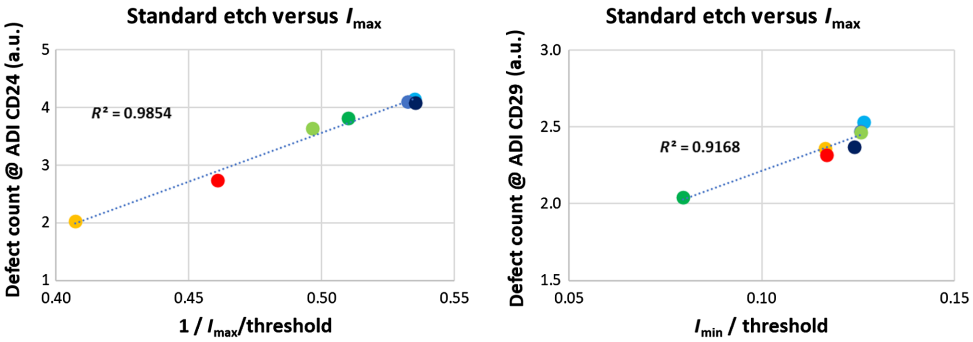


**Fig. 14** Correlation of defect rates (standard etch process and medium sensitivity inspection) with (a) the inverse of the aerial image maximum intensity over the threshold and (b) the minimum intensity over the threshold.

of larger systematic LCDU for inner sigma pupils is, therefore, evidence that mask roughness is dominated by small spatial frequencies.

No evidence for NFC-driven degradation of the LCDU at nominal conditions was seen, at least for the range tested here.

In terms of defectivity the defect levels correlated best with the maximum intensity over the threshold for missing holes and minimum intensity over the threshold for merging holes (Fig. 14). DoF appears to have little or no impact on defectivity for the nominal focus condition (etch process dependent). This would be beneficial for high-NA. However, caution must be applied as DoF will be more limited in 0.55 NA than what can be sampled in 0.33 NA. The improved maximum intensity and NILS in high-NA would lead to gains in LCDU and less missing holes. However, increasing the number of diffraction orders captured also results in higher minimum intensity and more merging holes.

In the end, based on the obtained results, the metrics are ranked in terms of their impact on defectivity in the following order: (1) minimum and maximum intensity over the threshold, (2) NILS, and (3) NFC. It should be noted that the intensity and the NILS are strongly correlated and increasing one will also increase the other. Furthermore, driving up the maximum intensity will also increase the minimum intensity if fading is not compensated. Each of the metrics impacts a different aspect of the contact hole. The intensities act predominantly on the center of the contact hole and the space between the contacts. The results seem to support the hypothesis that the increased number of photons in the center helps opening a developer path to the bottom of the feature, while reduced photon counts prevent resist lost in the space between features. NILS affects mostly the circumference of the holes where the edge is formed. A low NILS would lead to strong variability of the contact shape that in turn could promote the formation of defects. NFC can be pictured as NILS loss through the resist stack. Thick resists are typically used for the patterning of contact holes. Assume the best focus for the aerial image is positioned at the top of the hole. Then if NFC is high, NILS drops considerably over the depth of the resist profile leading to tapered side walls and possible scum formation at the bottom. Since AEI is performed, the etch process potentially alleviates this by breaking through the scum and straightening the sidewalls so that the impact of NFC appears small. Ultimately it would be interesting to repeat this study once high-NA imaging becomes experimentally available to verify whether the effect of the strongly increased NFC becomes more pronounced.

## Acknowledgments

The authors would like to thank David Rio from Brion for rendering the pupils. Parts of the manuscript were previously published as SPIE proceedings.[17]

## References

1. J. Van Schoot et al., "High-NA EUV lithography exposure tool: advantages and program progress," *Proc. SPIE* **11517**, 1151712 (2021).

2. P. de Bisschopand and E. Hendrickx, "On the dependencies of the stochastic patterning-failure cliffs in EUVL lithography," *Proc. SPIE* **11323**, 113230J (2020).
3. A. Erdmann et al., "Mask-induced best-focus shifts in deep ultraviolet and extreme ultraviolet lithography," *J. Micro/Nanolithogr. MEMS MOEMS* **15**(2), 021205 (2016).
4. J. Finders and J. Galvier, "Mask 3D induced phase and the mitigation by absorber optimization," *Proc. SPIE* **9426**, 942605 (2015).
5. J. Finders, L. de Winter, and T. Last, "Mitigation of mask three-dimensional induced phase effects by absorber optimization in ArFi and extreme ultraviolet lithography," *J. Micro/Nanolithogr. MEMS MOEMS* **15**(2), 021408 (2016).
6. J.-H. Franke et al., "Improving exposure latitudes and aligning best focus through pitch by curing M3D phase effects with controlled aberrations," *Proc. SPIE* **11147**, 111470E (2019).
7. M. Burkhardt et al., "Investigation of mask absorber induced image shift in EUV lithography," *Proc. SPIE* **10957**, 1095710 (2019).
8. J.-H. Franke et al., "Tomorrow's pitches on today's 0.33 NA scanner: pupil and imaging conditions to print P24 L/S and P28 contact holes," *Proc. SPIE* **11517**, 1151716 (2021).
9. J.-H. Franke et al., "Metal layer single EUV expose at pitch 28 nm: how bright field and NTD resist advantages align," *Proc. SPIE* **11609**, 116090R (2021).
10. L. Van Look et al., "Optimization and stability of CD variability in pitch 40 nm contact holes on NXE:3300," *Proc. SPIE* **10809**, 108090M (2018).
11. M.J. Maslow et al., "Impact of local variability on defect-aware process windows," *Proc. SPIE* **10957**, 109570H (2019).
12. G.F. Lorusso et al., "Roughness decomposition: an on-wafer methodology to discriminate mask, metrology and shot noise contributions," *Proc. SPIE* **10959**, 109590T (2019).
13. R. Jonckheere and L.S. Melvin, "Contribution of mask roughness in stochasticity of high-NA EUV imaging," *Proc. SPIE* **11854**, 118540I (2021).
14. R. Jonckheere and L.S. Melvin, "Stochastic printing behavior of non-local mask deficiencies in EUV lithography," *Proc. SPIE* **11517**, 1151710 (2020).
15. C. Mack, *Fundamental Principles of Optical Lithography: The Science of Microfabrication*, John Wiley & Sons, Chichester (2007).
16. P. Naulleau, Y.-G. Wang, and T. Pistor, "Extreme ultraviolet mask roughness effects in high numerical aperture lithography," *Appl. Opt.* **57**, 1724 (2018).
17. A. Frommhold et al., "Pupil optimization for after etch defectivity: what imaging metrics matter?" *Proc. SPIE* **11854**, 11854H (2021).

**Joern-Holger Franke** is an R&D engineer at IMEC. He obtained his PhD in the area of density functional theory from the University of Muenster, Germany, in 2010. After several post-docs, he joined IMEC focusing on EUV lithography, in 2015. His current research focuses on M3D effects in EUV imaging to better understand aerial image generation. Applications include source optimization including phase injection and pushing the resolution limit of current EUV scanners.

**Andreas Frommhold** is an R&D engineer at IMEC. He obtained his PhD in electrical engineering from the University of Birmingham, United Kingdom, in 2010. Afterward, he worked as a research fellow in chemical engineering at the same university on the development of photoresists and organic hard mask materials for semiconductor manufacturing. In 2016 he joined IMEC, where he is engaged in various research activities focusing on imaging and reticle-related aspects of EUV lithography.

**Mark Maslow** received his bachelor of science degree in microelectronic engineering from Rochester Institute of Technology, Rochester, New York, USA, in 1996. He spent 15 years working in the field of computational lithography before transitioning into studying the lithography and process transfer patterning impact on stochastic variability and defectivity. He currently lives and works in Eindhoven, The Netherlands as a system engineer for ASML. He has been an author on more than 20 research papers on topics ranging from computational lens heating, resist developer modeling, and most recently edge placement error.

Biographies of the other authors are not available.